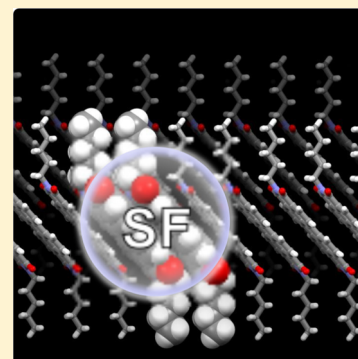


# Theoretical Investigation of Singlet Fission in Molecular Dimers: The Role of Charge Transfer States and Quantum Interference

Fatemeh Mirjani,\* Nicolas Renaud, Natalie Gorczak, and Ferdinand C. Grozema\*

Delft University of Technology, Julianalaan 136, 2628 BL Delft, The Netherlands

**ABSTRACT:** Singlet fission (SF) is a spin-allowed process by which a singlet excited state splits into a pair of triplet states. This process can potentially increase the efficiency of organic solar cells by a factor of 1.5. In this article, we study the dynamics of SF in different molecular aggregates of perylenediimide (PDI) derivatives, pentacene, and 1,3-diphenylisobenzofuran (DPB). To compute the SF rate, we have adopted a Markovian density matrix propagation approach to model SF in a molecular dimer. This approach allows accounting for both the coherent and incoherent processes that mediate the triplet formation. Our calculations show that SF can be much faster in PDI derivatives than in pentacene and DPB. Our analysis also indicates that SF is principally mediated by a superexchange mechanism that involves charge transfer states as virtual intermediates. In addition, because of the existence of different pathways for the formation of the triplet states, signatures of quantum interference are clearly observed.



## INTRODUCTION

Singlet fission (SF) is a spin-allowed process by which a singlet excited state converts into two triplet states.<sup>1–3</sup> This process is of interest for the design of chromophores for organic photovoltaics because it is possible, in principle, to inject two charges into an external circuit per absorbed photon.<sup>4–6</sup>

Singlet fission has been observed in different organic molecular crystals, such as pentacene,<sup>7,8</sup> tetracene,<sup>9</sup> 1,3-diphenylisobenzofuran,<sup>10,11</sup> perylenediimide (PDIs),<sup>12</sup> perylene,<sup>13</sup> benzophenone,<sup>14</sup> or rubrene.<sup>15</sup> As shown by extensive electronic structure calculations,<sup>16,17</sup> these molecules share a common feature: the energy of the singlet excited state is larger than twice the triplet energy, ( $E(S_1) > 2E(T_1)$ ). This energetic condition is crucial for SF because it allows the transition from the singlet to the double-triplet state to be exoergic. However, this energetic constraint is not the only parameter that determines the SF rate and yield, and it has been shown that the electronic couplings between the two neighboring molecules also play a significant role in the dynamics of the excited singlet state.<sup>16</sup>

Despite extensive efforts, the mechanism underlying SF remains unclear because two competing processes can be responsible for the triplet formation. The first process is a direct two-electron transfer in which the singlet state  $|S_0S_1\rangle$  or  $|S_1S_0\rangle$  produces two triplet states  $|T_1T_1\rangle$ :



This mechanism is characterized by a direct two-electron coupling matrix element  $t_{2e}$ , of which the magnitude strongly depends on the respective orientation of the two neighboring molecules.<sup>3</sup> As shown in Figure 1, the second mechanism, referred to as mediated transfer, uses the charge transfer states (CT) as either a real or virtual intermediate state for the formation of the pair of triplet states. In such a process, the

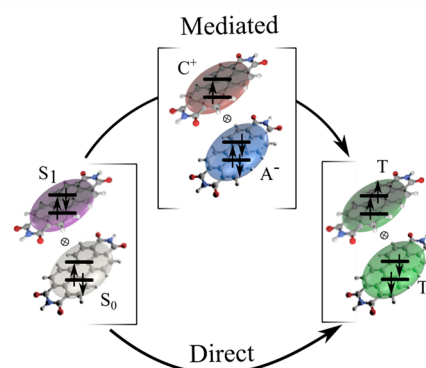
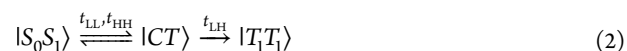


**Figure 1.** Schematic representation of two possible pathways to explain SF mechanism. The first mechanism is a direct two-electron transfer process in which the singlet state produces two triplet states. The second mechanism uses the charge transfer states for the formation of the double triplet states.

singlet state  $|S_0S_1\rangle$  or  $|S_1S_0\rangle$  converts to the triplet states via the charge transfer states:



The electronic coupling matrix elements  $t_{LL}$ ,  $t_{HH}$ , and  $t_{LH}$  are the LUMO–LUMO, HOMO–HOMO, and LUMO–HOMO one-electron couplings, respectively. As for  $t_{2e}$ , the magnitude of these couplings strongly depends on the mutual orientation of the molecules and can, in principle, be optimized by exploiting supramolecular self-assembly or by engineering of the crystal structure.<sup>18,19</sup>

Received: April 7, 2014

Revised: May 26, 2014

Published: June 6, 2014

Most of the previous theoretical work on SF indicates that the direct two-electron transfer dominates the SF mechanism,<sup>20–23</sup> however, a few theoretical studies based on the Redfield theory<sup>24,25</sup> or on ab initio calculations<sup>23</sup> have been made to determine the role of the CT states during the SF process. The results obtained from these studies indicate that the CT states can efficiently mediate the SF process via either a superexchange or a sequential electron transfer.<sup>24,25</sup>

In this contribution, we focus on aggregates of PDI molecules (see Figure 2) and study the relation between the

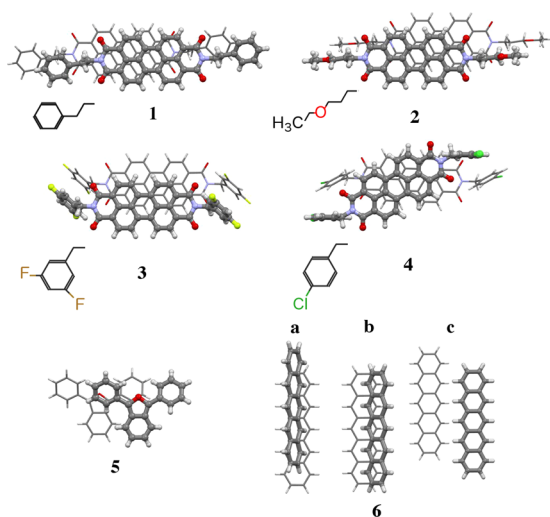


**Figure 2.** Structure of the molecular dimers studied here. (1–4) PDI derivatives, (5) 1,3-diphenylisobenzofuran (DPB), (6) pentacene.

stacking geometry of these molecules in the crystal and the SF rate. PDI derivatives are attractive candidates for SF because the triplet energy is almost exactly centered between the ground state and the lowest singlet excited state. In addition, PDIs form well-ordered  $\pi$ -stacked geometries that can be tuned by introducing different substituents to optimize the intermolecular electronic couplings.

Accounting for both the direct and mediated mechanism, Renaud et al.<sup>20</sup> have recently investigated the relation between stacking geometries and SF yield in PDI derivatives, using Marcus theory. Their results suggest that the dominant mechanism for SF in PDI aggregates is the direct two-electron mechanism. This work, however, neglects the possibility for the CT states to be used as a virtual intermediate path during the SF process, rather than a real intermediate that is fully populated. To account for this superexchange type transfer between the singlet and the double-triplet state, we examine in this paper the competition between the direct and mediated mechanism using Redfield theory.<sup>26–28</sup> Using this approach, we also study the relation between the stacking geometry and the SF rate and compare our results with the previous results based on the Marcus theory.<sup>20</sup> In addition, we have also studied SF for two other molecules, pentacene and 1,3-diphenylisobenzofuran (DPB), for which singlet fission has been observed experimentally (see Figure 2).

## DENSITY MATRIX PROPAGATION VIA THE REDFIELD THEORY

In this work, we have used Redfield theory,<sup>26–28</sup> which is a master-equation-based approach that assumes the system–bath coupling as a perturbation. The formalism starts from a

combined system–bath perspective from which a perturbative master equation is derived for the system alone, under the assumption of weak system–bath coupling. Redfield theory has recently been used to study the SF process in pentacene and tetracene.<sup>24,25,29</sup> Here, we apply this theory to molecules shown in Figure 2 by employing the secular approximation.<sup>28</sup> The latter prevents unphysical negative populations and guarantees that the system approaches a Boltzmann distribution in the long time limit.

In the Redfield formalism, the time-dependent density matrix elements,  $\rho_{ab}$ , are given by

$$\frac{d\rho_{ab}(t)}{dt} = -i\omega_{ab}\rho_{ab}(t) + \sum_{cd} R_{abcd}\rho_{cd}(t) \quad (3)$$

where

$$\omega_{ab} = \omega_a - \omega_b \quad (4)$$

are the eigenvalues of the system for the electron Hamiltonian  $H_{el}$  where

$$H_{el}|a\rangle = \omega_a|a\rangle \quad (5)$$

The first term on the right-hand side of eq 3 is responsible for the coherent energy transfer, whereas the second term represents the population relaxation and dephasing. The superoperator  $R$  in the second term is the Redfield operator calculated on the basis of the approach by Abramavicius et al.<sup>30</sup>

Within the secular approximation, diagonal elements of the density matrix  $\rho_{aa}$  that are representative of the population are obtained by

$$\frac{d\rho_{aa}(t)}{dt} = R_{aaaa}\rho_{aa}(t) - \sum_{b \neq a} R_{aabb}\rho_{bb}(t) \quad (6)$$

whereas the off-diagonal elements  $\rho_{ab}$  that contain information on the coherence are obtained by

$$\rho_{ab}(t) = \rho_{ab}(0) \exp(-i\omega_{ab}t) \exp(R_{abab}t) \quad (7)$$

The bath correlation functions including molecular vibrations, and phonons are described by a spectral density, which is assumed to have the form of an ohmic function<sup>31</sup>

$$J(\omega) = 2\lambda \frac{\omega\Omega}{\omega^2 + \Omega^2} \quad (8)$$

where  $\lambda$  is the reorganization energy and  $\Omega$  is the cutoff frequency. It should be noted that the bath spectral density can take other functional functions. Although recent reports indicate that variation of the spectral density does not affect the SF rate obtained for selected systems,<sup>24</sup> several articles have shown that a modification of the cutoff frequency of the spectral density can increase or decrease the energy transfer efficiency in biosystems and quantum dots trimers.<sup>32,33</sup>

The electronic structure of the active space used to model the molecular dimer where SF occurs can be represented by the Hamiltonian:

**Table 1.** Two-Electron and One-Electron Couplings (meV), and the Energies of Singlet, Charge Transfer and Triplet States (eV)

molecule	$t_{2e}$ (meV)	$t_{HH}$ (meV)	$t_{LL}$ (meV)	$t_{HL}$ (meV)	$E(CT)$ (eV)	$E(S_1)$ (eV)	$E(T_1)$ (eV)
1	−0.420	−125	145	−125	3.11	2.22	1.05
2	−1.650	−108	−14	−35	2.98	2.22	1.05
3	−0.001	−14	−100	0.8	3.39	2.22	1.05
4	−1.100	−35	22	2	3.52	2.22	1.05
5	0.510	15	−68	−33	4.06	2.61	1.26
6a	0.090	−48	−82	59	2.03	1.80	0.73
6b	−0.046	84	77	−51	2.03	1.80	0.73
6c	0.103	−34	−42	39	2.80	1.80	0.73

$$H = \begin{pmatrix} E(S_0S_1) & 0 & t_{LL} & -t_{HH} & t_{2e} \\ 0 & E(S_1S_0) & -t_{HH} & t_{LL} & t_{2e} \\ t_{LL} & -t_{HH} & E(CT) & 0 & \sqrt{\frac{3}{2}} t_{LH} \\ -t_{HH} & t_{LL} & 0 & E(CT) & \sqrt{\frac{3}{2}} t_{HL} \\ t_{2e} & t_{2e} & \sqrt{\frac{3}{2}} t_{LH} & \sqrt{\frac{3}{2}} t_{HL} & E(T_1T_1) \end{pmatrix} \quad (9)$$

The energies (diagonal terms) and electronic coupling matrix elements (off-diagonal terms) that enter the definition of this Hamiltonian can be extracted from density functional theory (DFT) and linear response time-dependent DFT (TDDFT) calculations, as will be presented in the next section.

## RESULTS AND DISCUSSIONS

**Electronic Couplings.** As is common in the literature on theoretical studies of singlet exciton fission,<sup>24,34,35</sup> the electronic coupling matrix elements,  $t_{XY}$  ( $X, Y = L, H$ ) that are present in eq 9 are approximated by one-electron integrals:

$$t_{XY} = \langle X | \mathcal{H}_{KS} | Y \rangle \quad (10)$$

where  $\mathcal{H}_{KS}$  is the Kohn–Sham Hamiltonian matrix of the molecular dimer. These off-diagonal matrix elements were computed using the fragment orbitals approach<sup>36</sup> in the Amsterdam Density Functional (ADF) package.<sup>37</sup> In these calculations, a TZ2P basis set and the B3LYP exchange–correlation functional were used to compute  $\mathcal{H}_{KS}$ . An orthogonalization procedure of the basis set was then employed to obtain the values of the adiabatic one-electron couplings reported in Table 1. These results are in excellent agreement with those obtained by Yamagata et al.<sup>38</sup>

As initially demonstrated by Jortner et al.,<sup>39</sup> the application of the Slater–Condon rules results in a compact expression of the two-electron couplings:

$$t_{2e} = \sqrt{\frac{3}{2}} \left( \langle L_1 L_2 | \frac{e^2}{r} | H_2 L_1 \rangle - \langle H_1 H_2 | \frac{e^2}{r} | L_2 H_1 \rangle \right) \quad (11)$$

where  $L_1$  and  $L_2$  are the LUMO of the first and second molecule in the dimer and  $H_1$  and  $H_2$  are the HOMO of these two molecules. To compute this electronic coupling value, the frontier molecular orbitals of both molecules were expanded in a Gaussian basis set, and the different two-electron integrals were computed following well-known numerical methods.<sup>40</sup> The values of the two-electron coupling element obtained for the dimers shown in Figure 2 are reported in Table 1. The

geometries of the dimers were taken from the known crystal structure of the compounds. As for the calculations of the two-electron transfer integrals, these values differ significantly among the different molecules and reach a maximum value of about 1.65 meV for 2.

**Excitation Energies.** The singlet and triplet excitation energies used to define the diagonal energies of the Hamiltonian were calculated using the TDDFT method for the different molecules shown in Figure 2. For all molecules considered, the triplet energy was found to be slightly lower than half of the singlet energy. The energies of the dimer were then approximated from these monomer calculations,<sup>16</sup> following  $E_{S_1S_0} = E(S_1)$  and  $E_{T_1T_1} = 2E(T_1)$  (see Table 1). This widely used approximation is similar in spirit to the uncoupled frozen density embedding (FDE) scheme.<sup>41</sup> Although FDE could be used to compute the energy of the CT states, we have here preferred a fully classical calculation based on the direct reaction field (DRF) force field.<sup>42</sup> In these calculations, we have embedded the system of interest, two neighboring molecules, in a crystalline environment of polarizable molecules. This method allows the explicit calculation of the polarization effects, including an electrostatic and an induction term. The electrostatic energy results from the static interaction between the charge distribution of the molecules. This term is proportional to  $1/r$ . The induction term is a direct result of the induced dipoles, that is, the energy cost needed to induce the dipoles as well as the interaction of the induced dipoles with the electrostatic field. To estimate the stabilization of the CT state by the polarizable surroundings, first, the charge distribution over a single molecule is simulated by atomic point charges that are fitted to the electrostatic potential derived from density functional theory calculation in the vacuum.<sup>43</sup> Afterward, the electrostatic and induction energies should be calculated for two different cases: (1) two neighboring molecules in the center of the cluster that are negatively and positively charged. (2) two neighboring molecules in the center of the cluster that are neutral. Once the electrostatic and induction energies for these two different cases are calculated, the CT state energy can be computed as

$$E(CT) = IP - EA + E_{elec} + E_{ind} \quad (12)$$

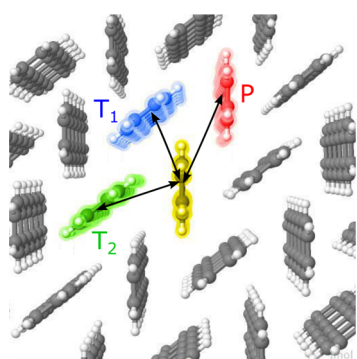
where IP and EA are the ionization potential and the electron affinity, respectively. These two quantities can be accurately evaluated using DFT calculations of the neutral and charged molecule. The values of the EA, IP, induction energy, and electrostatic energy obtained for the molecules studied here are reported in Table 2. As seen in this table, the induced dipoles always have an attractive interaction with the charges that induce them, and therefore, the induction interactions lead to the stabilization of the charged molecule compared with the

**Table 2.** Induction, Electrostatic, IP, EA, and CT State Energy Calculated by the DRF Method for Different Molecules

	$E_{\text{ind.}}$ (eV)	$E_{\text{elec.}}$ (eV)	IP (eV)	EA (eV)	$E(\text{CT})$ (eV)
1	−0.26	−1.93	7.62	2.32	3.11
2	−0.39	−1.96	7.68	2.35	2.98
3	−0.32	−1.71	7.90	2.48	3.39
4	−0.53	−1.14	7.63	2.44	3.52
5	−0.50	−2.13	6.84	0.15	4.06
6a	−0.69	−2.62	6.42	1.08	2.03
6b	−0.72	−2.59	6.42	1.08	2.03
6c	−0.62	−1.92	6.42	1.08	2.80

vacuum state. The electrostatic interaction with the surroundings can be, in general, either repulsive or attractive. In the values of the electrostatic energy in Table 2, the strong electrostatic interaction between the positively charged and negatively charged molecule are also included. The values reported here for the electrostatic energy are larger than the one obtained from the Mulliken population as previously reported by Renaud et al.<sup>20</sup>

Note that several values are reported for the pentacene crystals. This is due to the fact that there are three unique nearest neighbor dimers in the crystal,<sup>44</sup> as depicted in Figure 3: one configuration with the positively and negatively charged

**Figure 3.** Three different CT dimers in one layer of pentacene. The positively charged pentacene molecules (highlighted in yellow) can form a CT state with a negatively charged pentacene that is either oriented in parallel (P, in red), or transverse (T1, in blue, or T2, in green).

molecules oriented parallel with respect to each other (P), and two configurations transverse to each other (T1 and T2). Because of the similar configuration of T1 and T2, their electrostatic energy, which is mainly composed of the mutual attraction of the negative and positive charge, is almost identical. The electrostatic interaction of P amounts to ~74% of T1 and T2. This weaker interaction is a direct result of the larger distance between the molecules in P compared with T1 and T2. In comparison, the differences in the induction energy among the three dimers are significantly lower. Consequently, the CT state energy of T1 and T2 will be considerably lower than the CT state energy of P. Once the induction and electrostatic energies have been extracted from the DRF calculations, the CT energies for the molecule studied here can be calculated using eq 12. These values are shown in Table 2. Note that the values of the CT energy of PDIs obtained here are lower than the previously reported values of ~4.46 eV.<sup>20</sup> This is mainly due to the polarization of the molecules

surrounding the charged molecule in the dimer that tends to stabilize the CT states.

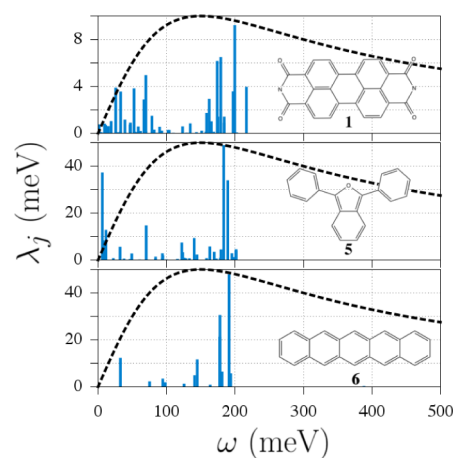
**Charge-Phonon Interactions.** The calculation of the different elements in the Redfield superoperator relies on the definition of the spectral density of the bath,  $J(\omega)$ , given in eq 8.<sup>30</sup> Although this allows for a straightforward evaluation of the relaxation and decoherence rate, an accurate estimation of the cutoff frequency,  $\Omega$ , and reorganization energy,  $\lambda$ , is needed. A possible solution to define these two parameters relies on the explicit calculation of the intramolecular charge phonon interaction on each individual molecule.<sup>29</sup>

A linear expansion of the energy of the frontier molecular orbitals with respect to the intramolecular vibrational coordinate leads to a simple expression for the mode-specific reorganization energy:<sup>45</sup>

$$\lambda_j = \frac{1}{2M_j\omega_j^2} \left( \frac{d\varepsilon_m}{dQ_m(j)} \right)_{Q=0}^2 \quad (13)$$

where  $\varepsilon_m$  is the energy of the state considered,  $M_j$  is the effective mass of the  $j$ th intramolecular vibrational mode,  $\omega_j$  is its frequency, and  $Q_m(j)$  is its vibrational coordinate. The interaction strength between a propagating charge and the  $j$ th vibrational mode of the molecule it resides on is, for example, obtained by using the LUMO energy as  $\varepsilon_m$ . Such calculations can be used to determine the cutoff frequency  $\Omega$  and the total reorganization energy as  $\lambda = \sum_j \lambda_j$ .<sup>29</sup>

To compute the values of  $\lambda_j$ , the geometry of each molecule was first relaxed using a DZP basis set and the LDA exchange-correlation functional. These fully relaxed geometries were then used to compute the vibrational modes of the molecules using the same basis set and functional. Subsequently, single-point calculations using a TZ2P basis set and the B3LYP exchange-correlation functional were performed to numerically evaluate the derivatives of the HOMO, LUMO, singlet, and triplet energies along each individual vibrational coordinate. The results of these calculations are shown in Figure 4. The results obtained for the 4 PDI derivatives were almost identical because the frontier molecular orbitals are localized on the core of the molecule, and therefore, the substituents only marginally change the results.<sup>19</sup> As already described elsewhere,<sup>46,47</sup> only vibrational modes of  $A_g$  symmetry couple with the electronic

**Figure 4.** Electron–phonon coupling for PDI (1), pentacene, and DPB. The sticks represent the mode-specific interaction strength. The dashed line shows the functional form of the bath spectral density.



level of PDI and pentacene because of the symmetry of their frontier molecular orbitals. Similarly, only vibration modes of A symmetry couple with the electronic level of DPB. Although the charge-phonon interaction can vary from one molecule to another, all the molecules exhibit pronounced interactions between the charge and the vibration modes centered around 0.15 eV. This value, which roughly corresponds to the C–C vibration mode, is therefore used to define the cutoff frequency of the bath spectral density,  $\Omega = 0.15$  eV, in the following. As seen in Table 3, the calculation of the total reorganization

**Table 3. Reorganization Energies for the Different Energies and Molecules Considered**

molecule	$\lambda_{\text{H}}$	$\lambda_{\text{L}}$	$\lambda_{\text{S1}}$	$\lambda_{\text{T1}}$
1	0.086	0.147	0.020	0.350
5	0.73	0.229	0.097	0.264
6	0.051	0.069	0.069	0.140

energy for the different energies considered here, that is, HOMO, LUMO, singlet, and triplet, shows large discrepancies. Consequently, we have fixed the value of the reorganization energy to their mean value,  $\lambda \approx 0.135$  eV. It should be noted that the values for  $\Omega$  and  $\lambda$  are in good agreement with previous estimations.<sup>24,20</sup>

**Triplet Formation Kinetics for Molecules 1–6.** Figure 5a shows the evolution of the population of the double-triplet state for molecules 1–6, as calculated using the Redfield methodology outlined above. As seen in this figure, the kinetics of the triplet formation varies significantly among the different molecules. To quantify this, the quantum yield ( $\Phi_{\text{SF}}$ ) and the rate constant  $k_{\text{SF}}$  of the SF process were evaluated by fitting the time-dependent population of Figure 5a with an exponential growth expression:  $\Phi(1 - \exp(-k_{\text{SF}}t))$ . Note that our theoretical SF yield does not account for the presence of other competing pathways, such as intersystem crossing, radiative and nonradiative decay to  $S_0$ , exciton fusion, and triplet relaxation, because these processes occur on a much longer time scale than the one explored here. The values of  $\Phi_{\text{SF}}$  and  $k_{\text{SF}}$  obtained via this fitting are reported in Table 4. As seen in this table, the largest SF rate is obtained for molecule 1 with  $k_{\text{SF}} = 79.0$  ps<sup>−1</sup>. For this molecule, rapid coherent oscillations with very small amplitude appears superimposed to the

exponential growth (see Figure 5b). In the extended limit, the population of different states in the system approaches a Boltzman distribution. The other PDI derivatives show slower triplet formation, with a minimum of  $k_{\text{SF}} = 0.56$  ns<sup>−1</sup> for molecule 3. The results are in good agreement with the available experimental results of Eaton et al.<sup>12</sup> for a PDI molecule that shows the formation of a triplet on the order of picoseconds. Our results indicate that the variation on stacking geometry of the two molecules in the dimer can significantly modify the kinetics of the SF process. A crystal engineering approach can therefore be adopted to finely tune the efficiency of the SF process.

The kinetics of the triplet formation for the reference compounds, DPB and pentacene, are also shown in Figure 5. As can be seen in this figure, DPB shows a SF rate of 0.31 ps<sup>−1</sup>, in agreement with experimental results that show the formation of triplet in few picoseconds.<sup>48</sup> The different geometries considered for the pentacene dimer lead to significantly different SF rates; hence, 6a and 6b present a high SF rate of  $\sim 1$  ps<sup>−1</sup>, whereas 6c shows a slow SF rate of a few nanoseconds<sup>−1</sup>. As seen in Table 2, the main difference between these dimers lies in the energy of the CT states. Therefore, our calculations underline the importance of these states for the SF process, even though they are never populated and act only as a virtual intermediate. It is interesting to note that the SF rates obtained here are slower than the experimental values of 12.5 ps<sup>−1</sup>.<sup>49</sup> This discrepancy might come from an underestimation of the electronic coupling or from the neglect of the intermolecular modes that may facilitate the SF mechanism. The latter is not unlikely, given the strong dependence of the electronic couplings on the mutual orientation of the two molecules.

It is interesting to note that the variations in  $k_{\text{SF}}$  follow the trend defined by the one-electron coupling  $t_{\text{HL}}$  shown in Table 1. For example, molecule 1 shows a very large value of  $t_{\text{HL}} = -0.125$  eV, whereas molecule 3 has a negligible coupling of 0.79 meV. This already indicates that the one-electron pathway via the CT intermediates is likely to influence the SF process in the PDI derivatives studied here. A similar conclusion has already been drawn in ref 23 as a result of an enhancement of the electronic couplings observed when allowing the CT state to mix with the singlet and triplet excited states.

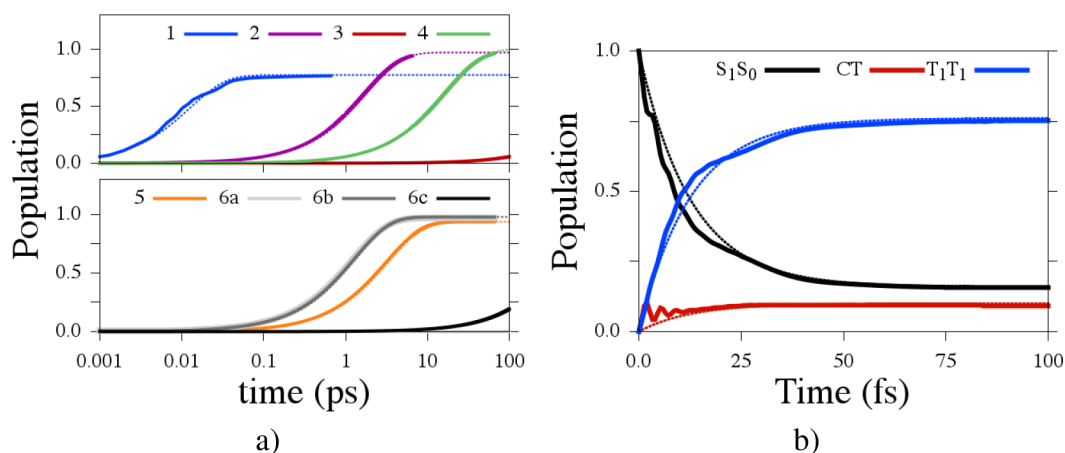


**Figure 5.** (a) Transient population of the double-triplet state obtained with the Redfield approach for the different molecules considered in this article. (b) Population of different states for molecule 1.

Table 4. SF Quantum Yield and Rate Constant ( $\text{ps}^{-1}$ ) for Molecules 1–6

	1	2	3	4	5	6a	6b	6c
$\Phi_{\text{SF}}$	0.79	0.97	0.99	1.0	0.94	0.98	0.98	0.90
$k_{\text{SF}}$	79.0	$5.5 \times 10^{-1}$	$5.6 \times 10^{-4}$	$5.6 \times 10^{-2}$	$3.1 \times 10^{-1}$	$7.7 \times 10^{-1}$	$7.5 \times 10^{-1}$	$2.5 \times 10^{-3}$

**Classical vs Quantum Transport in PDI Dimers: Superexchange and Interference.** In the previous study of SF in PDI derivatives,<sup>20</sup> the SF rate was computed via a Marcus approach in which the CT states are considered a real intermediate path of energy  $E(\text{CT}) = 4.46 \text{ eV}$ , that is, the CT is fully populated before progressing to the double-triplet state. Following that approach, the SF rate was calculated in the previous work<sup>20</sup> for different shifts along the short (dY) and long axis (dX) of the PDI molecule keeping an interplanar distance of 3.5 Å (see Figure 6a). The results of these

calculations are shown in Figure 7a. Note that for one-electron coupling, we have used the values reported by Renaud et al.<sup>20</sup> Moreover, we have recomputed here the values of the two-electron coupling with a greater accuracy than in ref 20 (see Figure 6b). This leads to significantly larger values of  $t_{2e}$  and, consequently, a higher SF rate that reaches  $2.0 \text{ ps}^{-1}$  in the most favorable geometry. As already concluded in ref 20, the direct mechanism dominates here as a result of the high energy of the CT states.

We have calculated the SF rate obtained via the Redfield equation for the different geometries of the PDI dimers. In these calculations, the energy of the CT states was kept to 4.46 eV. Figure 7b shows the variation of the SF rate with the stacking geometry of the PDI dimer. The difference between classical and quantum transport is striking. First of all, the quantum SF rate reaches a maximum value of  $40 \text{ ps}^{-1}$  instead of  $2.0 \text{ ps}^{-1}$  for the classical rate. In addition, the stacking geometries leading to a high SF rate are very different between the classical and quantum cases. This is due to the fact that the CT states can be used as virtual states during the propagation of the density matrix if the one-electron couplings are strong enough. This allows for a superexchange transfer between the  $S_1S_0$  and  $T_1T_1$  via the CT states, which is forbidden in the classical case.

According to our calculations, the strategy to optimize the SF rate consists therefore in finding the crystal structure that simultaneously optimizes all the one-electron couplings between the two neighboring molecules. Because the couplings  $t_{\text{HL}}$  and  $t_{\text{LH}}$  are null for two molecules stacked directly on top of each other, the SF rate can be non-null only for slip-stacked geometries. On the other hand, the couplings  $t_{\text{HH}}$  and  $t_{\text{LL}}$  are maximum when the molecules are on top of each other and progressively decreases for slip-stacked structures. The best geometry for SF corresponds, therefore, to a compromise between these two constraints. As for PDI, this optimal geometry corresponds to  $dY = 0$  and  $dX \approx 2.8 \text{ Å}$ .

To quantify the respective importance of both pathways, we have calculated the SF rate considering a single pathway at a time. The resulting maps obtained for the direct and mediated mechanism respectively are shown in Figure 8a. As seen in this figure, the SF rate obtained via the mediated mechanism only, referred to as  $\text{SF}_{\text{med}}$  in the following, reaches a maximum value of  $40 \text{ ps}^{-1}$  for similar stacking geometries of the total SF yield shown in Figure 7b. This confirms that the large values of the SF rate obtained by the Redfield theory are supported by the mediated mechanism only. In addition, note that the map of the SF rate, obtained via direct transfer only ( $\text{SF}_{\text{dir}}$ ), closely resembles the one using the Marcus theory.<sup>20</sup> This shows that the prediction of Marcus theory correctly accounts for the direct pathway but severely underestimates the role of the CT states.

A closer examination of the SF rates reveals that the total SF is not simply a sum of the rates of the two contributing pathways. The difference reveals the presence of quantum interference between the two different pathways. This interference effect is clearly shown in Figure 8b. In this figure, the variations of  $\text{SF}_{\text{tot}} - (\text{SF}_{\text{dir}} + \text{SF}_{\text{med}})$  are shown for the

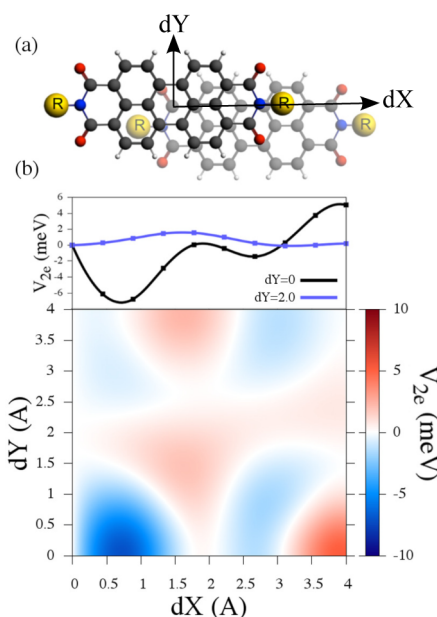


**Figure 6.** (a) Dimer of PDI slip-stacked shifted along the long and short axes of the molecule. dX and dY indicate the displacement along the X and Y axes. (b) Two-electron coupling for different geometries of the PDI dimers.

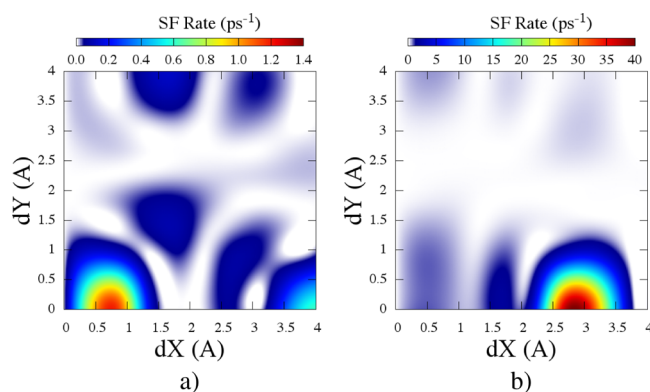


**Figure 7.** (a) Singlet fission rate obtained considering a classical transport, that is, the Marcus theory, as developed in ref 20. (b) Quantum transport described by a Redfield approach.

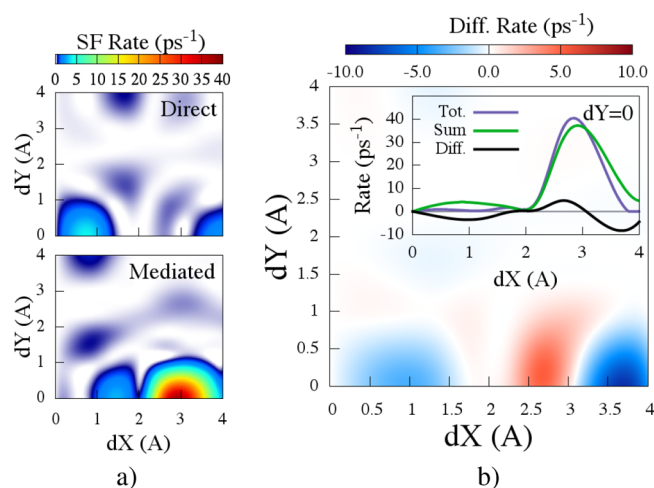


**Figure 8.** (a) SF rates obtained via the direct and mediated pathways. (b) Difference between the total rate and the sum of the individual pathways.

different stacking geometries of the dimer. Positive and negative regions, which correspond to constructive and destructive interference, respectively, clearly appear for small displacement along the short axis,  $dY$ . Quantum interference effects have previously been predicted<sup>50</sup> and experimentally observed<sup>51,52</sup> in the conduction in molecular junctions and have also been shown to play a role in electron transfer processes;<sup>53,54</sup> however, this is the first time, to the best of our knowledge, that their importance is predicted during SF. This interference pattern shows that the direct and the mediated pathways can either compete or cooperate during the excited state dynamics to enhance or reduce the SF rate.

## CONCLUSION

In this paper, we have investigated the SF process in PDI derivatives, pentacene, and 1,3-diphenylisobenzofuran. Our calculations were based on the time-dependent propagation of the density matrix in a restricted active space modeling a molecular dimer. The Redfield equation was used to account for both the coherent and the incoherent dynamics arising in this small active space. Our results show that SF occurs on a time scale of a few picoseconds in PDI derivatives, in agreement with experimental results. Our simulations also allowed us to identify the mechanism that mediates SF; hence, in the molecules studied in this article, SF occurs via the mediated pathway and not through the direct pathway. During the transfer from the singlet to the triplet state, the CT states are used as virtual intermediates and are never strongly populated. These results are in contrast with predictions obtained by the Marcus theory in which the CT states were considered as real intermediates and could not mediate a superexchange transfer. Our calculations also reveal the presence of quantum interference between the two different pathways; hence, the direct and mediated pathways can either cooperate or compete with each other during the SF process. Finally, our calculations show the influence that the stacking geometry of the molecular aggregate has on the SF rate. This underlines the structure–property relationship of the molecular crystal and paves the way to a crystal engineering approach for the design of efficient SF-based solar cells.

## AUTHOR INFORMATION

### Corresponding Authors

\*E-mail: fateme.mirjani@gmail.com.

\*E-mail: f.c.grozema@tudelft.nl.

### Notes

The authors declare no competing financial interest.

## REFERENCES

- (1) Singh, S.; Jones, W. J.; Siebrand, W.; Stoicheff, B. P.; Schneider, W. G. Laser Generation of Excitons and Fluorescence in Anthracene Crystals. *J. Chem. Phys.* **1965**, *42*, 330–342.
- (2) Smith, M. B.; Michl, J. Singlet Fission. *Chem. Rev.* **2010**, *110*, 6891–6936.
- (3) Smith, M. B.; Michl, J. Recent Advances in Singlet Fission. *Annu. Rev. Chem. Phys.* **2013**, *64*, 361–386.
- (4) Hanna, M. C.; Nozik, A. J. Solar Conversion Efficiency of Photovoltaic and Photoelectrolysis Cells with Carrier Multiplication Absorbers. *J. Appl. Phys.* **2006**, *100*, 074510.
- (5) Congreve, D. N.; Lee, J.; Thompson, N. J.; Hontz, E.; Yost, S. R.; Reusswig, P. D.; Bahlke, M. E.; Reineke, S.; Van Voorhis, T.; Baldo, M. A. External Quantum Efficiency Above 100 Organic Photovoltaic Cell. *Science* **2013**, *340*, 334–337.
- (6) Ehrler, B.; Walker, B. J.; Böhm, M. L.; Wilson, M. W. B.; Vaynzof, Y.; Friend, R. H.; Greenham, N. C. In situ measurement of exciton energy in hybrid singlet-fission solar cells. *Nat. Commun.* **2012**, *3*, 1019.
- (7) Ramanan, C.; Smeigh, A. L.; Anthony, J. E.; Marks, T. J.; Wasielewski, M. R. Competition between Singlet Fission and Charge Separation in Solution-Processed Blend Films of 6,13-Bis-(triisopropylsilyl)ethynyl)pentacene with Sterically-Encumbered Perylene-3,4,9,10-bis(dicarboximide)s. *J. Am. Chem. Soc.* **2012**, *134*, 386–397.
- (8) Wilson, M. W. B.; Rao, A.; Ehrler, B.; Friend, R. H. Singlet Exciton Fission in Polycrystalline Pentacene: From Photophysics toward Devices. *Acc. Chem. Res.* **2013**, *46*, 1330–1338.
- (9) Burdett, J. J.; Bardeen, C. J. Quantum Beats in Crystalline Tetracene Delayed Fluorescence Due to Triplet Pair Coherences Produced by Direct Singlet Fission. *J. Am. Chem. Soc.* **2012**, *134*, 8597–8607.
- (10) Scherwin, A. F.; et al. Toward Designed Singlet Fission: Electronic States and Photophysics of 1,3-Diphenylisobenzofuran. *J. Phys. Chem. A* **2010**, *114*, 1457–1473.
- (11) Johnson, J. C.; Nozik, A. J.; Michl, J. High Triplet Yield from Singlet Fission in a Thin Film of 1,3-Diphenylisobenzofuran. *J. Am. Chem. Soc.* **2010**, *132*, 16302–16303.
- (12) Eaton, S. W.; Shoer, L. E.; Karlen, S. D.; Dyar, S. M.; Margulies, E. A.; Veldkamp, B. S.; Ramanan, C.; Hartzler, D. A.; Savikhin, S.; Marks, T. J.; Wasielewski, M. R. Singlet Exciton Fission in Polycrystalline Thin Films of a Slip-Stacked Perylenediimide. *J. Am. Chem. Soc.* **2013**, *135*, 14701–14712.
- (13) Albrecht, W.; Michel-Beyerle, M.; Yakhot, V. Exciton Fission in Excimer Forming Crystal. Dynamics of an Excimer Build-up in Iso-perylene. *Chem. Phys.* **1978**, *35*, 193–200.
- (14) Katoh, R.; Kotani, M. Fission of a higher excited state generated by singlet exciton fusion in an anthracene crystal. *Chem. Phys. Lett.* **1992**, *196*, 108–112.
- (15) Najafov, H.; Lee, B.; Zhou, Q.; Feldman, L. C.; Podzorov, V. Observation of long-range exciton diffusion in highly ordered organic semiconductors. *Nat. Mater.* **2010**, *9*, 938.
- (16) Greyson, E. C.; Stepp, B. R.; Chen, X.; Scherwin, A. F.; Paci, I.; Smith, M. B.; Akdag, A.; Johnson, J. C.; Nozik, A. J.; Michl, J.; Ratner, M. A. Singlet Exciton Fission for Solar Cell Applications: Energy Aspects of Interchromophore Coupling. *J. Phys. Chem. B* **2010**, *114*, 14223.
- (17) Paci, I.; Johnson, J. C.; Chen, X.; Rana, G.; Popović, D.; David, D. E.; Nozik, A. J.; Ratner, M. A.; Michl, J. Singlet Fission for Dye-Sensitized Solar Cells: Can a Suitable Sensitizer Be Found? *J. Am. Chem. Soc.* **2006**, *128*, 16546–16553.



- (18) Vura-Weis, J.; Ratner, M. A.; Wasielewski, M. R. Geometry and Electronic Coupling in Perylene-3,4,9,10-tetracarboxylic Diimide Stacks: Mapping Structure–Charge Transport Relationships. *J. Am. Chem. Soc.* **2010**, *132*, 1738–1739.
- (19) Delgado, M. C. R.; Kim, E.-G.; Filho, D. A. d. S.; Brédas, J.-L. Tuning the Charge-Transport Parameters of Perylene Diimide Single Crystals via End and/or Core Functionalization: A Density Functional Theory Investigation. *J. Am. Chem. Soc.* **2010**, *132*, 3375–3387.
- (20) Renaud, N.; Sherratt, P. A.; Ratner, M. A. Mapping the Relation between Stacking Geometries and Singlet Fission Yield in a Class of Organic Crystals. *J. Phys. Chem. Lett.* **2013**, *4*, 1065–1069.
- (21) Zimmerman, P. M.; Zhang, Z.; Musgrave, C. B. Singlet Fission in Pentacene through Multi-Exciton Quantum States. *Nat. Chem.* **2010**, *2*, 648–652.
- (22) Zimmerman, P. M.; Bell, F.; Casanova, D.; Head-Gordon, M. Mechanism for Singlet Fission in Pentacene and Tetracene: From Single Exciton to Two Triplets. *J. Am. Chem. Soc.* **2011**, *133*, 19944–19952.
- (23) Havenith, R. W. A.; de Gier, H. D.; Broer, R. Explorative Computational Study of the Singlet Fission Process. *Mol. Phys.* **2012**, *110*, 2445–2454.
- (24) Berkelbach, T. C.; Hybertsen, M. S.; Reichman, D. R. Microscopic Theory of Singlet Exciton Fission. II. Application to Pentacene Dimers and the Role of Superexchange. *J. Chem. Phys.* **2013**, *138*, 114103.
- (25) Chan, W.-L.; Berkelbach, T. C.; Provorse, M. R.; Monahan, N. R.; Tritsch, J. R.; Hybertsen, M. S.; Reichman, D. R.; Gao, J.; Zhu, X.-Y. The Quantum Coherent Mechanism for Singlet Fission: Experiment and Theory. *Acc. Chem. Res.* **2013**, *46*, 1321–1329.
- (26) Redfield, A. G. On the Theory of Relaxation Processes. *IBM J. Res. Dev.* **1957**, *1*, 19–31.
- (27) Redfield, A. G. *Adv. Magn. Reson.* **1965**, *1*, 1.
- (28) Breuer, H. P.; Petruccione, F. *The Theory of Open Quantum Systems*; Oxford University Press: Oxford, 2003.
- (29) Berkelbach, T. C.; Hybertsen, M. S.; Reichman, D. R. Microscopic Theory of Singlet Exciton Fission. I. General Formulation. *J. Chem. Phys.* **2013**, *138*, 114102.
- (30) Abramavicius, D.; Palmieri, B.; Voronine, D. V.; Šanda, F.; Mukamel, S. Coherent Multidimensional Optical Spectroscopy of Excitons in Molecular Aggregates; Quasiparticle versus Supermolecule Perspectives. *Chem. Rev.* **2009**, *109*, 2350–2408.
- (31) Weiss, U. *Quantum Dissipative Dynamics*; World Scientific: Singapore, 1993.
- (32) Renaud, N.; Mujica, V.; Ratner, M. A. A Stochastic Surrogate Hamiltonian Approach of Coherent and Incoherent Exciton Transport in the Fenna–Matthews–Olson Complex. *J. Chem. Phys.* **2011**, *135*, 075102.
- (33) Pedromo, A.; Vogt, L.; Najmaie, A.; Aspuru-Guzik, A. Engineering Directed Excitonic Transfer. *Appl. Phys. Lett.* **2010**, *96*, 093114.
- (34) Greyson, E. C.; Vura-Weis, J.; Michl, J.; Ratner, M. A. Maximizing Singlet Fission in Organic Dimers: Theoretical Investigation of Triplet Yield in the Regime of Localized Excitation and Fast Coherent Electron Transfer. *J. Phys. Chem. B* **2010**, *114*, 14168–14177.
- (35) Teichen, P. E.; Eaves, J. D. A Microscopic Model of Singlet Fission. *J. Phys. Chem. B* **2012**, *116*, 11473–11481.
- (36) Senthikumar, K.; Grozema, F. C.; Bickelhaupt, F. M.; Siebbeles, L. D. A. Charge Transport in Columnar Stacked Triphenylenes: Effects of Conformational Fluctuations on Charge Transfer Integrals and Site Energies. *J. Chem. Phys.* **2003**, *119*, 9809–9817.
- (37) ADF2013, SCM, Theoretical Chemistry, Vrije Universiteit, Amsterdam, The Netherlands, <http://www.scm.com>.
- (38) Yamagata, H.; Norton, J.; Hontz, E.; Olivier, Y.; Beljonne, D.; Brédas, J. L.; Silbey, R. J.; Spano, F. C. The nature of singlet excitons in oligoacene molecular crystals. *J. Chem. Phys.* **2011**, *134*, 204703.
- (39) Jortner, J.; Rice, S. A.; Katz, J. L.; Choi, S.-I. Triplet Exciton in Crystals of Aromatic Molecules. *J. Chem. Phys.* **1965**, *42*, 309.
- (40) Taketa, H.; Huzinaga, S.; Oohata, K. Gaussian-Expansion Methods for Molecular Integrals. *J. Phys. Soc. Jpn.* **1966**, *21*, 2313–2324.
- (41) Wesolowski, T. A.; Warshel, A. Frozen Density Functional Approach for Ab Initio Calculations of Solvated Molecules. *J. Phys. Chem.* **1993**, *97*, 8050–8053.
- (42) Swart, M.; van Duijnen, P. T. DRF90: A Polarizable Force Field. *Mol. Sim.* **2006**, *32*, 471–484.
- (43) Gorczak, N.; Swart, M.; Grozema, F. C. Energetics of Charges in Organic Semiconductors and at Organic Donor–Acceptor Interfaces. *J. Mater. Chem. C* **2014**, *2*, 3467–3475.
- (44) Siegrist, T.; Besnard, C.; Haas, S.; Schiltz, M.; Pattison, P.; Chernyshov, D.; Batlogg, B.; Kloc, C. A Polymorph Lost and Found: The High-Temperature Crystal Structure of Pentacene. *Adv. Mater.* **2007**, *19*, 2079–2082.
- (45) Coropceanu, V.; Cornil, J.; da Silva Filho, D. A.; Olivier, Y.; Silbey, R.; Brédas, J.-L. Charge Transport in Organic Semiconductors. *Chem. Rev.* **2007**, *107*, 926–952.
- (46) Kato, T.; Yamabe, T. Vibronic Interactions and Superconductivity in Acene Anions and Cations. *J. Chem. Phys.* **2001**, *115*, 8592–8602.
- (47) Girlando, A.; Grisanti, L.; Masino, M.; Brillante, A.; Della Valle, R. G.; Venuti, E. Interaction of Charge Carriers with Lattice and Molecular Phonons in Crystalline Pentacene. *J. Chem. Phys.* **2011**, *135*, 084701.
- (48) Johnson, J. C.; Nozik, A. J.; Michl, J. High triplet Yield from Singlet Fission in a Thin Film of 1,3-Diphenylisobenzofuran. *J. Am. Chem. Soc.* **2010**, *132*, 16302.
- (49) Wilson, M. W. B.; Rao, A.; Ehrler, B.; Friend, R. H. Singlet Exciton Fission in Polycrystalline Pentacene: From Photophysics toward Devices. *Acc. Chem. Res.* **2013**, *46*, 1330–1338.
- (50) Sautet, P.; Joachim, C. Electronic Interference Produced by a Benzene Embedded in a Polyacetylene Chain. *Chem. Phys. Lett.* **1988**, *153*, 511–516.
- (51) Guedon, C. M.; Valkenier, H.; Markussen, T.; Thygesen, K. S.; Hummelen, J. C.; van der Molen, S. J. *Nat. Nanotechnol.* **2012**, *7*, 305–309.
- (52) Arroyo, C. R.; Tarkuc, S.; Frisenda, R.; Seldenthuis, J. S.; Woerde, C. H. M.; Eelkema, R.; Grozema, F. C.; van der Zant, H. S. J. Signatures of Quantum Interference Effects on Charge Transport Through a Single Benzene Ring. *Angew. Chem., Int. Ed.* **2013**, *52*, 3152–3155.
- (53) Patoux, C.; Coudret, C.; Launay, J.-P.; Joachim, C.; Gourdon, A. Topological Effects on Intramolecular Electron Transfer via Quantum Interference. *Inorg. Chem.* **1997**, *36*, 5037–5049.
- (54) Renaud, N.; Powell, D.; Zarea, M.; Movaghar, B.; Wasielewski, M. R.; Ratner, M. A. Quantum Interferences and Electron Transfer in Photosystem I. *J. Phys. Chem. A* **2013**, *117*, 5899–5908.